Science
AAAS

Metallic Quantum Well States in Artificial Structures of Strongly Correlated Oxide

K. Yoshimatsu, *et al.*

Science **333**, 319 (2011);
DOI: 10.1126/science.1205771

superficially similar to convective models in some respects (*28*) but nevertheless fail to explain the origin and energy flux of this structure (*4*–*8*, *28*) as well as the present observations.

References and Notes

1. J. Evershed, *Mon. Not. R. Astron. Soc.* **69**, 454 (1909).
2. R. Schlichenmaier, K. Jahn, H. U. Schmidt, *Astrophys. J.* **493**, L121 (1998).
3. R. Schlichenmaier, S. K. Solanki, *Astron. Astrophys.* **411**, 257 (2003).
4. H. C. Spruit, G. B. Scharmer, *Astron. Astrophys.* **447**, 343 (2006).
5. G. B. Scharmer, H. C. Spruit, *Astron. Astrophys.* **460**, 605 (2006).
6. M. Rempel, M. Schüssler, M. Knölker, *Astrophys. J.* **691**, 640 (2009).
7. M. Rempel, M. Schüssler, R. H. Cameron, M. Knölker, *Science* **325**, 171 (2009).
8. M. Rempel, *Astrophys. J.* **729**, 5 (2011).
9. T. Heinemann, Å. Nordlund, G. B. Scharmer, H. C. Spruit, *Astrophys. J.* **669**, 1390 (2007).
10. G. B. Scharmer, Å. Nordlund, T. Heinemann, *Astrophys. J.* **677**, L149 (2008).
11. K. Ichimoto *et al.*, *Science* **318**, 1597 (2007).
12. J. Sánchez Almeida, I. Márquez, J. A. Bonet, I. Dominguez Cerdeña, *Astrophys. J.* **658**, 1357 (2007).
13. V. Zakharov, J. Hirzberger, T. L. Riethmüller, S. K. Solanki, P. Kobel, *Astron. Astrophys.* **488**, L17 (2008).
14. H. C. Spruit, G. B. Scharmer, M. G. Löfdahl, *Astron. Astrophys.* **521**, A72 (2010).
15. G. B. Scharmer *et al.*, *Astrophys. J.* **689**, L69 (2008).
16. The spectra were constructed from a total of 960 images sampling 23 wavelengths in typical steps of 28 mÅ plus 480 wideband images. The images were processed with multi-object, multiframe blind deconvolution image restoration techniques (*29*, *30*) to reduce the effects of residual aberrations in the images.
17. G. B. Scharmer, K. Bjelksjö, T. K. Korhonen, B. Lindberg, B. Petterson, *Proc. SPIE* **4853**, 341 (2003).
18. R. Schlichenmaier, W. Schmidt, *Astron. Astrophys.* **349**, L37 (1999).
19. J. de la Cruz Rodríguez, D. Kiselman, M. Carlsson, *Astron. Astrophys.* **528**, A113 (2011).
20. Additional figures and more detailed information about the straylight estimation and compensation, influence of molecular blends, the estimation of average radial and downflow velocities and circular polarization, and the correlation between intensities, velocities, and magnetic field inclinations are available as supporting material on *Science* Online.
21. S. Danilovic *et al.*, *Astron. Astrophys.* **484**, L17 (2008).
22. S. K. Mathew, V. Zakharov, S. K. Solanki, *Astron. Astrophys.* **501**, L19 (2009).
23. S. Wedemeyer-Böhm, L. Rouppe van der Voort, *Astron. Astrophys.* **503**, 225 (2009).
24. G. B. Scharmer, B. V. Gudiksen, D. Kiselman, M. G. Löfdahl, L. H. van der Voort, *Nature* **420**, 151 (2002).
25. B. W. Lites, D. F. Elmore, P. Seagraves, A. P. Skumanich, *Astrophys. J.* **418**, 928 (1993).
26. M. Franz, R. Schlichenmaier, *Astron. Astrophys.* **508**, 1453 (2009).
27. L. R. Bellot Rubio, R. Schlichenmaier, K. Langhans, *Astrophys. J.* **725**, 11 (2010).
28. G. B. Scharmer, *Space Sci. Rev.* **144**, 229 (2009).
29. M. G. Löfdahl, *Proc. SPIE* **4792**, 146 (2002).
30. M. van Noort, L. Rouppe van der Voort, M. G. Löfdahl, *Sol. Phys.* **228**, 191 (2005).

Acknowledgments: P. Sütterlin provided valuable support during the observations and data analysis, and B. Edvardsson provided advice concerning line blends. J.d.l.C.R. gratefully acknowledges financial support by the European Commission through the SOLAIRE Network (MTRN-CT-2006-035484). CRISP was funded by the Marianne and Marcus Wallenberg Foundation. The Swedish 1-meter Solar Telescope is operated on the island of La Palma by the Institute for Solar Physics of the Royal Swedish Academy of Sciences in the Spanish Observatorio del Roque de los Muchachos of the Instituto de Astrofísica de Canarias.

Supporting Online Material

www.sciencemag.org/cgi/content/full/science.1206429/DC1
Materials and Methods
Figs. S1 to S21
Tables S1 to S9
References (*31*–*39*)

4 February 2011; accepted 25 May 2011
Published online 2 June 2011;
10.1126/science.1206429

Metallic Quantum Well States in Artificial Structures of Strongly Correlated Oxide

K. Yoshimatsu,[1] K. Horiba,[1,2] H. Kumigashira,[1,2,3]*† T. Yoshida,[4] A. Fujimori,[4] M. Oshima[1,2,5]

The quantum confinement of strongly correlated electrons in artificial structures provides a platform for studying the behavior of correlated Fermi-liquid states in reduced dimensions. We report the creation and control of two-dimensional electron-liquid states in ultrathin films of $SrVO_3$ grown on Nb:$SrTiO_3$ substrates, which are artificial oxide structures that can be varied in thickness by single monolayers. Angle-resolved photoemission from the $SrVO_3$/Nb:$SrTiO_3$ samples shows metallic quantum well states that are adequately described by the well-known phase-shift quantization rule. The observed quantum well states in $SrVO_3$ ultrathin films exhibit distinctive features—such as orbital-selective quantization originating from the anisotropic orbital character of the V 3*d* states and unusual band renormalization of the subbands near the Fermi level—that reflect complex interactions in the quantum well.

An electron confined in space by a potential well forms standing waves in the well, or quantum well (QW) states. These states are characterized by the quantum number n, that is, the number of half-wavelengths that span the well. QW states are associated with discrete quantized electronic states in thin artificial structures with tunable physical dimensions, in which electron confinement occurs only in the direction perpendicular to the surface, giving rise to two-dimensional (2D) QW states. Metallic QW states are similar to those known in semiconductor structures, except that the shorter Fermi wavelength allows spatially narrower confinement of high-density electrons (*1*–*6*). The metallic QW states are realized in QW structures based on metals having nearly free-electron–like *sp* states, such as Ag/Si (*5*), Pb/Si (*6*), and noble metals on metal substrates (*1*–*4*). The resultant 2D electronic structures have been intensively studied by using angle-resolved photoemission spectroscopy (ARPES) (*1*–*6*).

Depending on the number of conductive layers, layered complex oxides that are both low-dimensional and strongly interacting often exhibit unusual physical properties, such as high-temperature superconductivity in cuprates, triplet superconductivity in ruthenates, and enhancement of colossal magnetoresistance in manganites (*7*). The properties originate from stacked conductive layers, which strongly correlated electrons, sandwiched by block insulating layers. The lowering of the dimensionality changes the interaction among the spin, charge, and orbital degrees of freedom. However, systematic control of the dimensionality while keeping the fundamental electronic parameters fixed has not yet been conducted, owing to the difficulties in the synthesis of a homologous series of layered complex oxides (*7*).

The close structural similarities of layered oxides to metallic QW structures have motivated researchers to create low-dimensional systems in a controllable fashion using artificial structures of a strongly correlated oxide. That is, the artificial oxide structures provide a setting in which to study the behavior of strongly correlated electrons in reduced dimensions and to control the extraordinary physical properties of strongly correlated oxides (*8*). Although the carrier confinement at the interface of oxide semiconductors has been reported (*9*, *10*), the metallic QW states having the dimensional controllability has not been achieved yet in oxide artificial structures.

We chose $SrVO_3$ ultrathin films epitaxially grown on Nb-doped $SrTiO_3$ (Nb:STO) as a possible candidate for creating QW states having 2D electron-liquid states. $SrVO_3$ is a typical Fermi-liquid metal with the simple $3d^1$ configuration (*7*, *11*–*13*), and its electronic structures can be simulated by use of the Hubbard model without

[1]Department of Applied Chemistry, University of Tokyo, Bunkyo-ku, Tokyo 113-8656, Japan. [2]Synchrotron Radiation Research Organization, University of Tokyo, Bunkyo-ku, Tokyo 113-8656, Japan. [3]Precursory Research for Embryonic Science and Technology (PRESTO), Japan Science and Technology Agency (JST), Kawaguchi, Saitama 332-0012, Japan. [4]Department of Physics, University of Tokyo, Bunkyo-ku, Tokyo 113-0033, Japan. [5]Core Research for Evolutional Science and Technology (CREST), JST, Bunkyo-ku, Tokyo 113-8656, Japan.

*To whom correspondence should be addressed. E-mail: kumigashira@sr.t.u-tokyo.ac.jp
†Present address: Photon Factory, Institute of Materials Structure Science, High Energy Accelerator Research Organization (KEK), 1-1 Oho, Tsukuba 305-0801, Japan.

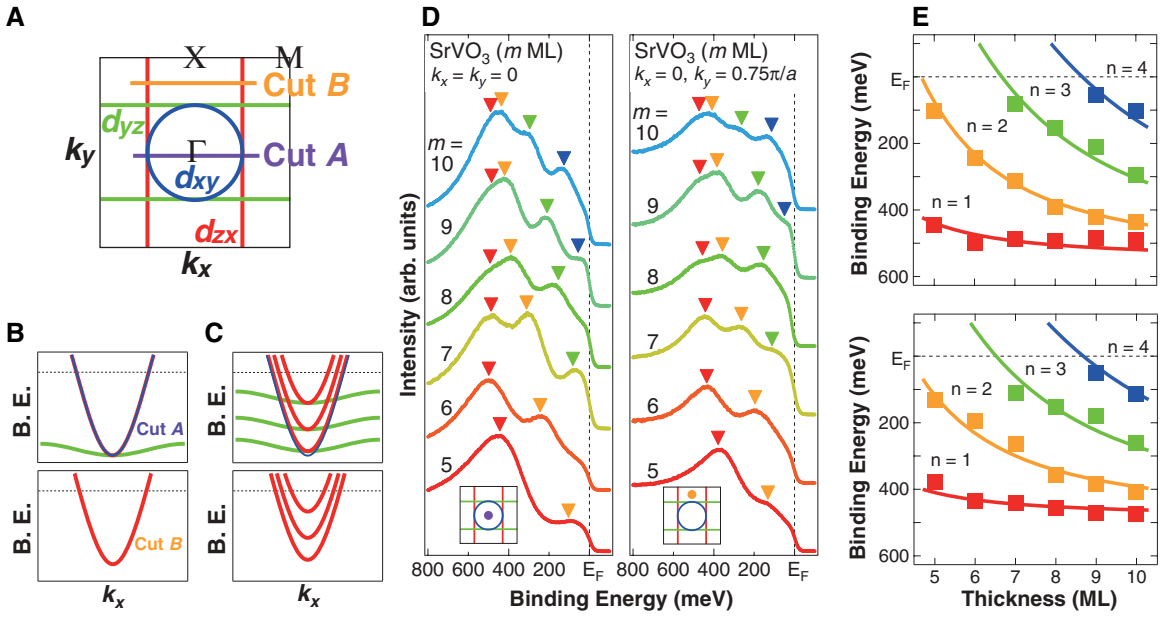

Fig. 1. (**A**) FS cross sections in the Γ*XM* ($k_z = 0$) plane of $SrVO_3$. The FS consists of three cylindrical FS sheets originating from three V 3*d* bands: d_{xy} (blue), d_{yz} (green), and d_{zx} (red) (fig. S2) (*16*). The measurement lines (cuts *A* and *B*) of the present ARPES are also shown. (**B**) Band dispersions of bulk $SrVO_3$ predicted from band structure calculations (*17*) for cuts *A* and *B*. (**C**) Quantization states in $SrVO_3$ ultrathin films expected from the band structure. Orbital-selective quantization occurs, reflecting the anisotropic character of V 3*d* states. The resultant subband dispersions are illustrated for cuts *A* and *B*. (**D**) ARPES spectra of $SrVO_3$ ultrathin films varying the film thickness obtained at points (0, 0) (left) and (0, 0.75π/*a*) (right). The peak structures derived from QW states are marked by the colored triangles. (**E**) Structure plots showing the energy positions of corresponding QW-state peaks (data markers) versus the film thickness for points (0, 0) (top) and (0, 0.75π/*a*) (bottom). The solid lines are predictions for the QW states (with $n = 1$ to 4) from the phase-shift quantization model (*1*–*6*, *16*).

explicit consideration of the oxygen *p* orbital (*14*). The metallic V 3*d* states located near the Fermi level (E_F) in $SrVO_3$ ultrathin films are expected to be highly confined in the QW structures formed between the vacuum (surface) and the Nb:STO substrate (interface) because Nb:STO has a large band gap of 3.2 eV below E_F (*15*, *16*). Our previous angle-integrated PES studies on $SrVO_3$/Nb:STO revealed that the metallic V 3*d* states near E_F are located within the band gap of Nb:STO, although strong electron correlation in the $SrVO_3$ ultrathin films manifests itself in the metal-insulator transition (MIT) that occurs at a critical film thickness of 2 to 3 monolayers (ML) (*15*).

The Fermi surface (FS) sheets of bulk $SrVO_3$ with cubic symmetry (fig. S2) (*16*) are essentially formed from three intersecting cylinders containing the V 3*d* d_{xy}, d_{yz}, and d_{zx} states (*16*, *17*). Each state has a 2D character in the *xy*, *yz*, and *zx* planes, respectively. The 2D nature of each state causes the FSs in the Γ*XM* emission plane (the $k_x - k_y$ plane, with $k_z = 0$) to consist essentially of two parallel lines originating from d_{zx} and d_{yz} states and a circular FS from the d_{xy} state (Fig. 1A) (*16*–*20*). The band structures along the Γ–*X* direction (cut *A*) consist of three bands: two degenerate parabolic dispersions derived from the d_{xy} and d_{zx} states and a nearly nondispersive d_{yz} state (*16*–*20*). However, the band dispersion along the *X*–*M* direction (cut *B*) is described by one parabolic band from the d_{zx} state (Fig. 1B). When the $SrVO_3$ film becomes sufficiently thin along the *z* direction to realize the quantum confinement of V 3*d* electrons in the film, the bands derived from d_{zx} and d_{yz} are expected to form quantized states because these orbitals expand along the *z* direction. On the other hand, the d_{xy} state remains unchanged because of its 2D character in the *xy* plane. Thus, the quantized d_{yz} and d_{zx} states and one bulk-like d_{xy} state are expected to be observed for cut *A*, whereas simple quantized states derived from the d_{zx} orbital are expected for cut *B* (Fig. 1C).

Certain aspects of 2D QW states in metal films have been studied by use of ARPES (*1*–*6*). By measuring ARPES spectra, the energy position of each quantization state and the in-plane energy dispersion of the confined electrons were obtained directly. Figure 1D shows the ARPES spectra for $SrVO_3$ ultrathin films varying in overlayer thickness obtained at the (0, 0) and (0, 0.75π/*a*) points in the Γ*XM* emission plane. The energy positions of the several quasiperiodic peaks evolved as a function of overlayer thickness: With increasing thickness, one additional peak appears after another in the ARPES spectra at E_F, and their peak positions shift to higher binding energies. The peak shift apparently converged around 500 meV, which corresponds to the bottom of the V 3*d* conduction bands (*18*–*20*). The spectral changes suggest the formation of metallic QW states in $SrVO_3$/Nb:STO.

In order to show the dependence of the quantized electronic states on the film thickness more clearly, we plotted the binding energies as a function of the $SrVO_3$ film thickness (Fig. 1E). For quantitative analysis, we invoked the usual phase-shift quantization rule, which has been used successfully in the interpretation of metallic QW states in noble metal systems (*1*–*6*, *16*). The solid lines in Fig. 1E represent the calculated results for the QW states. Comparing the experimental and calculated data, the experimental binding energies are fairly well reproduced by calculations based on the phase-shift quantization rule. This good agreement indicates that the metallic V 3*d* states located near E_F in $SrVO_3$ are confined in the QW structures.

The orbital-selective quantization of the QW states could be seen in the in-plane band dispersion determined with ARPES. The band dispersion of the subbands formed for an 8-ML $SrVO_3$ ultrathin film is shown in Fig. 2. As expected from the illustration in Fig. 1C, two types of subbands were observed for the band dispersion along cut *A* (Fig. 2A); one is the parabolic band, which approaches and eventually crosses E_F with increasing distance from the Γ point, whereas the other is the nearly flat band. These two bands are degenerate at the Γ point. However, only parabolic subbands were observed along cut *B* (Fig. 2B). Considering the anisotropic orbital nature of the 3*d* states, the flat bands seen only in Fig. 2A and the parabolic band seen in both cases originate from the quantized d_{yz} and d_{zx} states, respectively. From the structure plots shown in Fig. 1E, the quantum number of each subband is $n = 1$, 2, and 3 from the bottom. Because the original d_{zx} and d_{xy} states are degenerate along the Γ–*X* direction (Fig. 1B), the band dispersion of the first quantized d_{zx} state almost overlaps with that of the bulk-like d_{xy} state because their bottom energies are nearly equal. The existence of the original d_{xy}

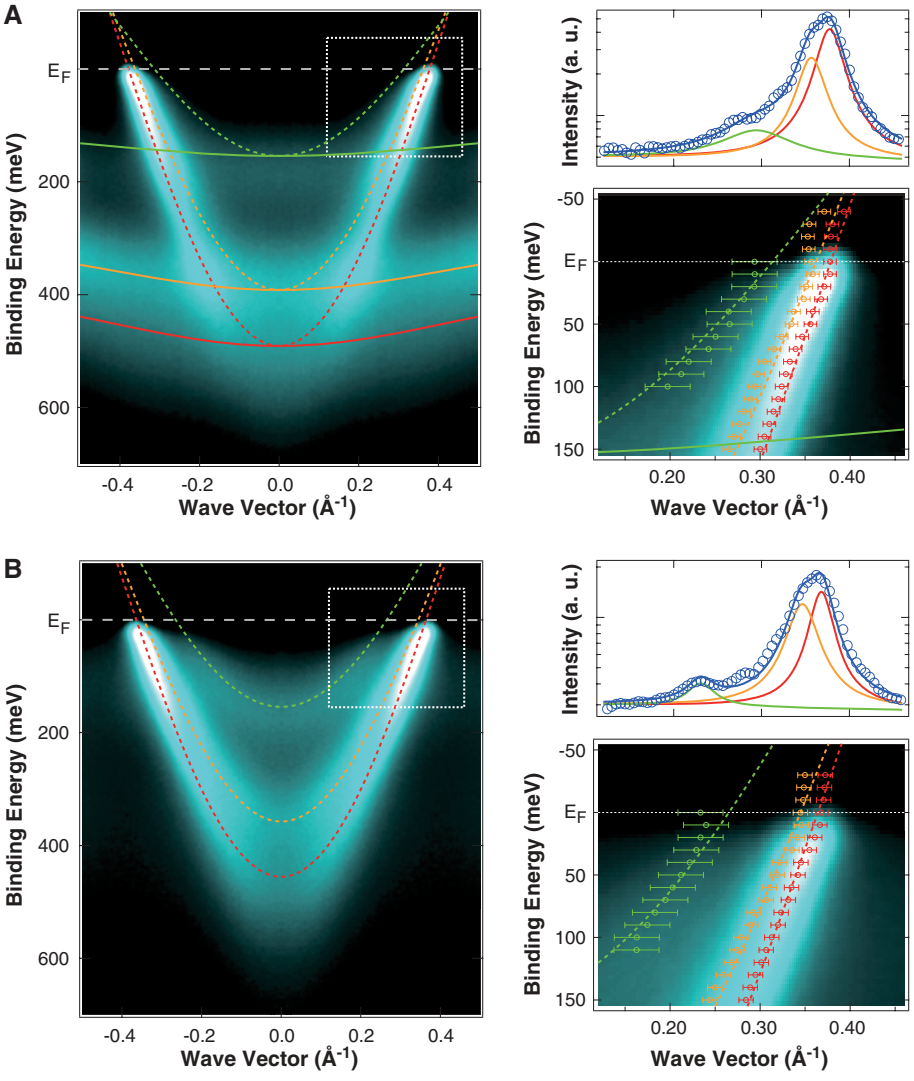

Fig. 2. Orbital-selective quantization of V 3*d* states in $SrVO_3$ ultrathin films. (**A** and **B**) Intensity plots of ARPES spectra for 8-ML $SrVO_3$ ultrathin films for cuts *A* (A) and *B* (B). The intensity plots are symmetrized with respect to the center line and averaged (figs. S5 to S9) (*16*). The dashed and solid lines present the fitted curves to the dispersion using Eq. 1 for the d_{zx} and d_{yz} quantization states, respectively. Red, orange, and green lines correspond to states in which n = 1, 2, and 3, respectively. Magnifications of the boxes to the left are shown correspondingly to the right, together with the momentum distribution curve (MDC) at E_F with an energy window of ±5 meV. The blue line for each MDC curve is the sum of three Lorentzians corresponding to the respective subbands. The peak positions determined from MDCs are shown by the open circles (figs. S10 to S12) (*16*).

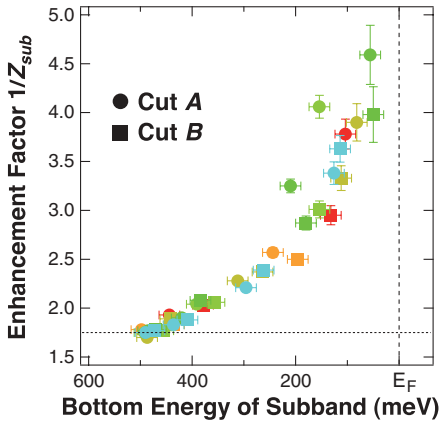

Fig. 3. Plots of the enhancement factor ($1/Z_{sub}$) for respective QW subbands as a function of their bottom energy for various $SrVO_3$ film thicknesses. The data marker colors correspond to those of the respective ARPES spectra shown in Fig. 1D.

band irrespective of the quantization of d_{yz} and d_{zx} bands was confirmed through ARPES measurements by using dichroic effects along different cuts where the degeneracy was lifted (*16*).

Although the quantization reflecting the anisotropic V 3*d* states itself is expected from band structure calculation, orbital-selective quantization has important implications for thickness-dependent MIT in $SrVO_3$ ultrathin films (*15*). $SrVO_3$ ultrathin films underwent a thickness-dependent phase transition from metal to insulator at a film thickness of less than 4 ML. In the structure plot (fig. S4) (*16*), the quantization states did not exist in occupied states below 2 ML. This thickness corresponds to the critical thickness at which MIT occurs in $SrVO_3$ thin films, suggesting that the thickness-dependent MIT in $SrVO_3$ ultrathin films is related to the orbital-selective quantization effect.

Lastly, there is the band renormalization of subbands located near E_F. In the in-plane dispersion of the subbands shown in Fig. 2, the subband dispersion becomes narrower with approaching its bottom energy to E_F. For quantitative discussion, the band renormalization factor (Z_{sub}) is evaluated with a least-squares fitting of the subband dispersion by using the following equation

$$E_{sub}(k_{//}) = Z_{sub}E^{TB}(k_{//}) + \varepsilon^* \qquad (1)$$

where $E^{TB}(k)$ is the band dispersion calculated by using the tight-binding parameters (*16*, *17*). Only Z_{sub} and ε^* are adjustable parameters so as to fit the in-plane dispersion of the subbands. As can be seen in Fig. 2, the fitted curves by using Eq. 1 adequately reproduce the in-plane dispersion of the subbands.

The relation between the enhancement factor ($1/Z_{sub}$) and the binding energy of the quantization states is summarized in Fig. 3. As the binding energy of quantization states approaches E_F, the effective mass of the subbands is considerably enhanced. Such a mass enhancement has not been observed in QW structures based on metals having nearly free-electron–like states (*1*–*6*). We conclude that the mass enhancement in the subbands is associated with strong interaction among V 3*d* electrons confined in the QW structures (*8*, *11*–*13*). There is one feature of the band renormalization that seems to contradict with the Fermi-liquid picture: If each subband can be described as a simple Fermi liquid, subbands located at lower binding energies should have weaker band narrowing owing to the reduction of correlation effects with reduced band filling (*21*). The unusual band renormalization may be related to the complicated interactions induced by the reduction of dimensionality, such as orbital selective Mott transition (*22*) and orbital and/or electronic reconstruction at the surface and the interface, but this issue remains to be resolved.

References and Notes

1. T.-C. Chiang, *Surf. Sci. Rep.* **39**, 181 (2000).
2. M. Milun, P. Pervan, D. P. Woodruff, *Rep. Prog. Phys.* **65**, 99 (2002).
3. R. K. Kawakami *et al.*, *Nature* **398**, 132 (1999).
4. J. J. Paggel, T. Miller, T.-C. Chiang, *Science* **283**, 1709 (1999).
5. I. Matsuda, T. Ohta, H.-W. Yeom, *Phys. Rev. B* **65**, 085327 (2002).
6. Y. Guo *et al.*, *Science* **306**, 1915 (2004).
7. M. Imada, A. Fujimori, Y. Tokura, *Rev. Mod. Phys.* **70**, 1039 (1998).
8. S. Okamoto, A. J. Millis, *Nature* **428**, 630 (2004).
9. A. Ohtomo, D. A. Muller, J. L. Grazul, H. Y. Hwang, *Nature* **419**, 378 (2002).
10. A. Ohtomo, H. Y. Hwang, *Nature* **427**, 423 (2004).

11. I. H. Inoue, O. Goto, H. Makino, N. E. Hussey, M. Ishikawa, *Phys. Rev. B* **58**, 4372 (1998).
12. I. H. Inoue *et al.*, *Phys. Rev. Lett.* **74**, 2539 (1995).
13. I. A. Nekrasov *et al.*, *Phys. Rev. B* **73**, 155112 (2006).
14. A. Georges, G. Kotliar, W. Krauth, M. J. Rozenberg, *Rev. Mod. Phys.* **68**, 13 (1996).
15. K. Yoshimatsu *et al.*, *Phys. Rev. Lett.* **104**, 147601 (2010).
16. Materials and methods are available as supporting material on *Science* Online.
17. E. Pavarini, A. Yamasaki, J. Nuss, O. K. Andersen, *N. J. Phys.* **7**, 188 (2005).
18. M. Takizawa *et al.*, *Phys. Rev. B* **80**, 235104 (2009).
19. T. Yoshida *et al.*, *Phys. Rev. Lett.* **95**, 146404 (2005).
20. T. Yoshida *et al.*, *Phys. Rev. B* **82**, 085119 (2010).
21. W. F. Brinkman, T. M. Rice, *Phys. Rev. B* **2**, 4342 (1970).
22. M. Neupane *et al.*, *Phys. Rev. Lett.* **103**, 097001 (2009).

Acknowledgments: The authors are very grateful to I. Matsuda, S. Okamoto, and M. J. Rozenberg for useful discussions and K. Ono and A. Yagishita for their support in the experiment at the Photon Factory (PF), KEK. This work was supported by a Grant-in-Aid for Scientific Research (A19684010 and S22224005) from the Japan Society for the Promotion of Science (JSPS) and the JST PRESTO program. K.Y. acknowledges the financial support from JSPS for Young Scientists. This work at KEK-PF was done under the approval of the Program Advisory Committee (proposals 08S2-003 and 09S2-005) at the Institute of Materials Structure Science, KEK.

Supporting Online Material

www.sciencemag.org/cgi/content/full/333/6040/319/DC1
Materials and Methods
SOM Text
Figs. S1 to S15
References

17 March 2011; accepted 25 May 2011
10.1126/science.1205771

Explosive Percolation Is Continuous

Oliver Riordan*† and Lutz Warnke*

"Explosive percolation" is said to occur in an evolving network when a macroscopic connected component emerges in a number of steps that is much smaller than the system size. Recent predictions based on simulations suggested that certain Achlioptas processes (much-studied local modifications of the classical mean-field growth model of Erdős and Rényi) exhibit this phenomenon, undergoing a phase transition that is discontinuous in the scaling limit. We show that, in fact, all Achlioptas processes have continuous phase transitions, although related models in which the number of nodes sampled may grow with the network size can indeed exhibit explosive percolation.

The quintessential example of a phase transition in statistical physics is the emergence of the giant component in the mean-field random graph: Erdős and Rényi (*1*) discovered that in a graph or network constructed in a completely (uniformly) random manner, as the ratio between the number m of edges (also called links) and the number n of vertices (nodes) passes ½, there is a dramatic change in the component (connectivity) structure. More precisely, if $m \sim tn$, where t represents time, for $t < ½$, the number C of nodes in the largest connected component is logarithmic in n, whereas for $t > ½$, C is of order n: A macroscopic component emerges at the critical time $t_c = ½$; this component is known as the giant component, even when its size is a small constant times n. Taking the natural scaling limit, there is a function $\rho(t) = \rho^{ER}(t)$ given by a simple formula such that $C \sim \rho(t)n$ when $m \sim tn$, with $\rho(t) > 0$ if and only if $t > ½$.

The Erdős-Rényi (ER) model and its phase transition are of fundamental importance for two main reasons. Mathematically, the properties of this phase transition are extremely well understood, including the fine details of the behavior at and near the critical point, and the dynamics of the transition [see, for example, (*1*–*5*)]. This model serves as the natural reference point when studying a wide range of phase transitions in mathematics and statistical physics: Similarities to and differences from the mean-field model are key to understanding more complex and perhaps less tractable models.

Second, random graphs are the natural mathematical models for complex or disordered networks in the real world. The mean-field model is unlikely to be appropriate itself for any particular application, but intuition from its study is the starting point for understanding more recent network models, such as the scale-free models of Barabási and Albert (*6*) and many others. Studying the emergence of large-scale connectedness as an edge-density parameter is varied corresponds to varying the proportion of links in an existing network that fail, and asking whether it remains connected on a large scale (*7*, *8*). Alternatively, thinking of the links as contacts that may spread a disease, the emergence of a giant component corresponds to epidemic spread of a disease rather than localized outbreaks (*9*, *10*).

For the reasons above, phase transitions in random graph models of many types have been widely studied [see the many references in (*11*)]. A key question is, how do the transitions in the different models relate? Which features are specific to the model, and which are universal? In 2007, Bollobás, Janson, and Riordan (BJR) (*11*) introduced a very general family of models that includes many special cases previously studied. They showed that for each model M in this family, there is a function $\rho^M(t)$ describing the rescaled size of the giant component; this function is zero up to some critical value t_c (which may be 0) and positive for $t > t_c$. For all models in the BJR family, $\rho^M(t)$ is continuous, but a huge range of different behaviors near t_c is possible (Fig. 1). For any critical exponent $\gamma \geq 1$, examples are given in (*11*) with $\rho^M(t_c + \varepsilon) \sim A\varepsilon^\gamma$ as $\varepsilon \to 0$, where A is a constant. Infinite order transitions also occur in natural models, with $\rho^M(t_c + \varepsilon) \approx \exp(-1/\sqrt{\varepsilon})$ [see (*12*) and the references therein].

With continuity of the function ρ seeming to be the only property that does not change from one model to the next, it was extremely exciting when Achlioptas, D'Souza, and Spencer (*13*) announced that a rather simple dynamical modification of the ER model seemed to undergo a discontinuous phase transition, a phenomenon now known as explosive percolation. Here, we show that this is not the case. Our argument is relatively

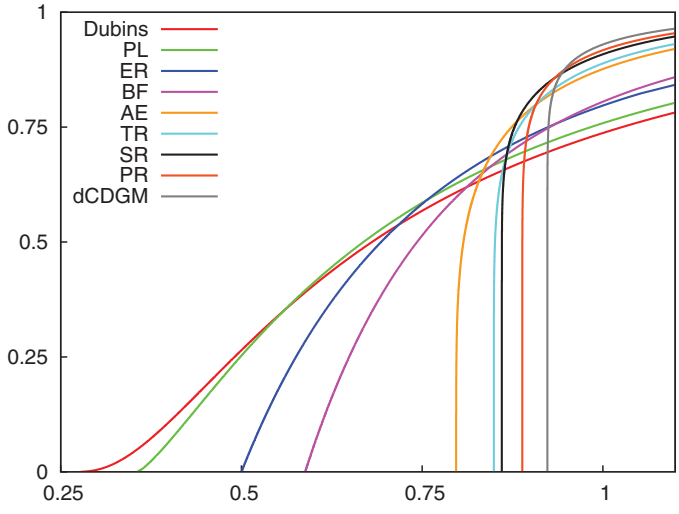

Fig. 1. The scaling limit of the giant component size, for various random graph models. The ER, power-law (PL), and Dubins models fall in the BJR family. The BF rule, SR, and PR are Achlioptas processes; the adjacent edge (AE) rule (*23*), triangle rule (TR) (*23*), and dCDGM (*26*) are Achlioptas-like processes. The figure is based on simulations with $n = 10^9$ (PL and Dubins) or $n = 10^{12}$ vertices. The last five curves appear to be discontinuous at the critical point, but this is not the case.

Mathematical Institute, University of Oxford, 24–29 St Giles', Oxford OX1 3LB, UK.

*These authors contributed equally to this work.
†To whom correspondence should be addressed. E-mail: riordan@maths.ox.ac.uk